

Article

Behavior of Corroded Thin-Walled Concrete-Filled Steel Tubular Stub Columns

Wen Xue ¹, Ju Chen ², Fang Xie ^{3,*}, Changhu Ye ² and Chengbin Liu ²

¹ Department of Civil Engineering, Zhejiang University of Science and Technology, Hangzhou 310023, China; xuewen@zust.edu.cn

² Department of Civil Engineering, Zhejiang University, Hangzhou 310058, China; cecj@zju.edu.cn (J.C.); ycheciv@yeah.net (C.Y.); lcb@zju.edu.cn (C.L.)

³ Department of Civil Engineering, Shaoxing University, Shaoxing 312000, China

* Correspondence: xiefangusx@163.com; Tel.: +86-137-3536-9940; Fax: +86-575-8834-8565

Abstract: The behavior of two series of corroded thin-walled concrete-filled steel tubes (CFSTs) was investigated in this paper. One series, called the CT series, consists of fourteen CFST specimens corroded by NaCl solution, while the other, called the AT series, consists of six test pieces corroded in the atmosphere. Outer surfaces of corroded steel tubes were scanned using a 3D scanner machine, and a complete surface profile of each specimen was obtained for corrosion evaluation using different methods in this study. Entire test pieces were compressed to failure, and their behaviors under loading were recorded. It is shown that corrosion has a fractal feature, and it has a significant effect on the ductility of specimens. In addition, FEA models of corroded CFST specimens were established based on the 3D scanning profile results using the ABAQUS program and verified against column test results.

Keywords: concrete-filled steel tubes; corrosion; stub columns; 3D scanning



Citation: Xue, W.; Chen, J.; Xie, F.; Ye, C.; Liu, C. Behavior of Corroded Thin-Walled Concrete-Filled Steel Tubular Stub Columns. *Buildings* **2022**, *12*, 481. <https://doi.org/10.3390/buildings12040481>

Academic Editor: Eva O. L. Lantsoght

Received: 19 March 2022

Accepted: 8 April 2022

Published: 13 April 2022

Publisher's Note: MDPI stays neutral with regard to jurisdictional claims in published maps and institutional affiliations.



Copyright: © 2022 by the authors. Licensee MDPI, Basel, Switzerland. This article is an open access article distributed under the terms and conditions of the Creative Commons Attribution (CC BY) license (<https://creativecommons.org/licenses/by/4.0/>).

1. Introduction

Concrete-filled steel tubes (CFSTs) have been widely used recently due to their high performance, such as in bridge structures, offshore structures, and electric transmission towers [1–8]. These structures suffer from corrosion due to environmental attack, especially from chloride ingress. The thickness of steel tubes decreased compared with traditional steel structures, thanks to the contribution of concrete; this could result in a significantly high corrosion rate at the usual corrosion depth. Therefore, it is important to investigate the effect of corrosion on the behavior of CFST structures.

Behavior of corroded CFST specimens under axial loading [9], sustained loading [10], tension [11], and eccentric loading [12,13] were investigated by Han et al. Corrosion of CFST specimens was accelerated by electrochemical method in 3.5% NaCl solution. Finite element simulation of the corroded CFST specimens was also conducted by Han et al. [10–13], where the uniform corrosion of steel tubes was simulated by reducing the stiffness of the corroded steel elements. Deterioration of the bond stress between the steel and the concrete interface, as well as concrete performance, were also considered. Research results indicated that the CFST specimens were generally uniformly corroded under the electrochemical accelerating method. The thickness of the steel tube decreased due to corrosion, which led to a reduction in the constraint effect on concrete. Furthermore, the buckling resistance of the steel tube also decreased.

Corrosion of steel structural elements has been investigated for decades. Nowadays innovative methods have been used, such as a 3D scanning method for corrosion of structural steel [14], aluminum alloy [15], bridge wires [16], and butt-welded joints [17]. The coordinate data of a corroded surface is usually obtained by this 3D scanning method, and thus, the geometry size of the remaining part would be accurately described. Parameters,

such as the maximum depth of corrosion pits, the area of pits, and the shape of pits, could be obtained by data analysis [17]. Meanwhile, it has been shown that 3D scanning results can be used to establish the finite element of corroded tensile coupon specimens and that the cracks in the corroded tensile coupon specimens could be predicted using the FEA model by incorporating the ductile fracture criterion of steel. Based on the aforementioned, this study is going to use the 3D scanning method to analyze the situation of the corroded CFST specimens and, simultaneously, to establish their corresponding FEA models.

A total of 20 test pieces, including 14 CFST specimens corroded by 5 wt % NaCl solution and 6 CFST specimens corroded in atmosphere, without external applied current, were investigated in this study, in order to obtain the similar corrosion condition in engineering reality. Structural steel grade Q235 and Q420, as well as concrete grades C35, C50, and C60, were used. The outer surfaces of all steel tubes are prepared by using 3D scanner machine. Then, all test specimens are compressed under axial loading. In addition, FEA models of the corroded CFST specimens become established and verified against test results. Finally, the suitability of the current design methods are evaluated against test and numerical results.

2. Experimental Program

2.1. Test Specimen Configuration

In this study, concrete filled in the steel tube before welding the top ending plate. Test specimens are labelled such that the type and time of the corrosion, as well as concrete grade, could be identified from the label. For example, the label “CT90C60B” defines the specimens as follow:

- The first letter indicates the type of corrosion, where the prefix letter “C” refers to chloride corrosion, and “A” refers to the atmospheric corrosion.
- The following letter, “T”, with two digits “90”, indicates the corrosion time in days.
- The following letter, “C”, with two digits “60”, refers to the concrete grade.
- The last character, “B”, refers to the repeated test piece.

2.2. Materials

2.2.1. Concrete and Steel Tubes

The concrete elastic modulus (E_c) and compressive strength (f_{cu}) obtained on 150-mm cubes at 28 days are presented in Table 1. The material properties of the steel tubes were obtained through tensile coupon tests. The coupons were taken from the same batch of steel tubes as the column test specimens in the longitudinal direction. The 12.5-mm-wide coupon dimensions conformed to Australian Standard AS 1391 [18] for tensile testing of metals. A displacement-controlled test machine with friction grips was used for the coupon tensile test in accordance with AS 1391 [18]. A calibrated 50-mm gauge length extensometer was used to measure the tensile strain. The values for Young’s modulus (E_s), yield stress (F_y), and ultimate tensile strength (F_u), based on the coupon test results, are shown in Table 2.

2.2.2. Specimen Design

A total of 20 CFST column specimens were designed, among which 14 specimens were prepared for the chloride corrosion condition, namely the CT series, and the other 6 were prepared for atmospheric corrosion condition, namely the AT series, as shown in Table 3. Seamless steel tubes, labeled S, and welded steel tubes, labeled W, were prepared for the CT series and AT series, respectively. The geometry and dimensions of the concrete-filled steel tubes are presented in Table 3 using the symbols plotted in Figure 1. For the CT series, two 15-mm-thick steel plates were welded on opposite ends with the purpose of preventing the chloride solution from affecting the inner surface of column specimens, while for the AT series, each has one 15-mm-thick steel plate welded on end for the convenience of scanning, as seen in Figure 2. For the AT series, there are four 50 × 6 mm angle bars inside the concrete considering the preparation method in Xu et al. [2]. Those angles have no effect on the corrosion of the AT specimens according to previous research.

Table 1. Material properties of concrete.

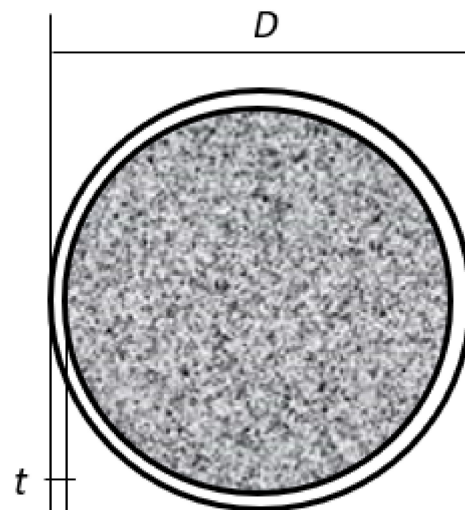
Component	Test Value		
Concrete grade	C35	C50	C60
E_c (MPa)	31,420	34,230	35,574
f_{cu} (MPa)	34.8	51.9	54.8

Table 2. Material properties of steel.

Component	CT Series	AT Series
Nominal thickness/diameter (mm)	4.0	6.0
Yield strength F_y (MPa)	460.0	280.9
Ultimate strength F_u (MPa)	640.0	4.0
Young's modulus E_s (MPa)	1.98×10^5	2.03×10^5

Table 3. Test specimens.

Specimens	Concrete	T (Day)	D_t (mm)	t (mm)	L (mm)	Tube
CT0C35	C35	0	160	4	480	S
CT0C60	C60	0	160	4	480	S
CT30C35	C35	30	160	4	480	S
CT30C60	C60	30	160	4	480	S
CT60C35	C35	60	160	4	480	S
CT60C60	C60	60	160	4	480	S
CT90C35A	C35	90	160	4	480	S
CT90C35B	C35	90	160	4	480	S
CT90C60A	C60	90	160	4	480	S
CT90C60B	C60	90	160	4	480	S
CT120C35A	C35	120	160	4	480	S
CT120C35B	C35	120	160	4	480	S
CT120C60A	C60	120	160	4	480	S
CT120C60B	C60	120	160	4	480	S
AT1100C50A	C50	1100	300	6.0	1000	W
AT1100C50B	C50	1100	300	6.0	1000	W
AT1100C50C	C50	1100	300	6.0	1000	W
AT1100C50D	C50	1100	300	6.0	1000	W
AT1100C50E	C50	1100	300	6.0	1000	W
AT1100C50F	C50	1100	300	6.0	1000	W

**Figure 1.** Cross section of CFST specimens.



(a)



(b)

Figure 2. Corroded CFST specimens: (a) specimens corrosion accelerated by NaCl (CT series); (b) specimens corrosion in atmosphere (AT series).

2.3. Corrosion Process

Neither the AT series nor the CT series were coated on the outer surface of the steel tubes in this study. The AT specimens were simply placed in the laboratory after a casting of concrete for about 1100 days. Afterwards, scanning detection was carried out. Dust on the test pieces was manually removed before the process of scanning. The CT specimens were exposed to a chloride erosion environment where 5 wt % NaCl solution was sprayed on the outer surface of the steel tubes six times every day. Specimens of the CT series were divided into four batches according to the sprayed time of 30, 60, 90, and 120 days. Deruster was used to remove the dust before scanning.

2.4. 3D Scanning Process

Shining 3D-Scanner equipment with the accuracy of 0.015–0.035 mm was used for the specimens' outer surface corrosion tests as shown in Figure 3. Scanning was performed after the rust cleaning process was performed on the test specimens. An area of 200 mm × 150 mm could be scanned each time to form a figure of the surface profile. Multiple scanned figures could be merged into a complete surface profile of a specimen, as shown in Figure 4a. The coordinate data of each spot were obtained from the scanning results, as shown in Figure 4b.

2.5. Loading and Data Acquisition

The test rig and the test set-ups are shown in Figure 5. A 10,000 kN hydraulic testing machine was used to apply compressive axial force to the column specimens by the displacement control at a rate of 1.0 mm/min. Three LVDTs (linear variable differential transformers) were positioned on the top end plate of the column specimen to measure the axial shortening. In addition, eight strain gauges were attached at mid-length of the columns to measure the strain. Four strain gauges were attached vertically, while the other four strain gauges were attached horizontally. A data acquisition system was used to record the readings of the strain and the compressive load at regular intervals during the tests.



Figure 3. Scanning of corroded CFST specimens.

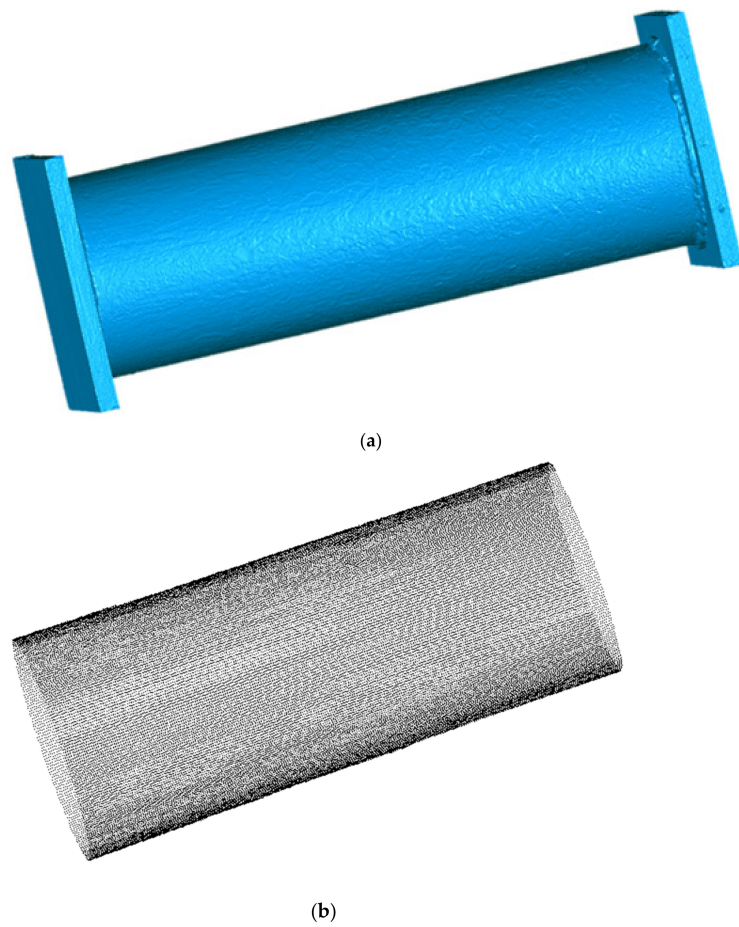


Figure 4. Surface profile and coordinate data obtained from 3D scanning results: (a) surface profile; (b) coordinate data.



Figure 5. Load tests.

3. Test Results

3.1. Corrosion Evaluation

Current ASTM Standard G46 [19] provided the method for evaluation of corrosion based on its density, size, and pit depth. Evaluation results of corrosion pits on the outer surface of the specimens were presented in Table 4. It is found that the corrosion evaluation of the ASTM results was approximately the same for each individual series. According to ASTM Standard G46, A-2, B-5 and C-1 are evaluated as carrion for the CT series, except for the individuals CT30C60 and CT90C60B, while the result is A-3, B-5 and C-3 for the entire AT series. It is reasonable for the AT specimens have close results thanks to their significantly identical corrosion condition. Nevertheless, the density, size, and depth of the corrosion pits are a little different for the CT test pieces, which might indicate a relatively short corrosion time, as one of the corrosion conditions is weakened once among the complete test condition parameters.

Table 4. Corrosion evaluation of specimens.

Specimens	Density	Size (mm ²)	Depth (mm)	ASTM Results	Ψ (%)	D
CT30C35	180	28.27	0.35	A-2, B-5, C-1	2.93	2.2867
CT30C60	200	10.56	0.4	A-2, B-4, C-1	1.05	2.2981
CT60C35	190	25.5	0.45	A-2, B-5, C-1	7.56	2.3659
CT60C60	230	20.43	0.4	A-2, B-5, C-1	10.35	2.3263
CT90C35A	150	30.11	0.6	A-2, B-5, C-1	9.19	2.3724
CT90C35B	130	45.37	0.55	A-2, B-5, C-1	10.07	2.3696
CT90C60A	124	19.63	0.4	A-2, B-5, C-1	1.36	2.2847
CT90C60B	195	12.23	0.35	A-2, B-4, C-1	1.99	2.2878
CT120C35A	200	22.12	0.45	A-2, B-5, C-1	7.91	2.3247
CT120C35B	195	24.63	0.5	A-2, B-5, C-1	8.99	2.3294
CT120C60A	140	37.39	0.6	A-2, B-5, C-1	11.91	2.3453
CT120C60B	160	35.56	0.5	A-2, B-5, C-1	9.43	2.3080
AT1100C50A	500	24.52	1–2	A-3, B-5, C-3	27.2	2.4226
AT1100C50B	400	26.34	1–2	A-3, B-5, C-3	31.0	2.3031
AT1100C50C	400	25.03	1–2	A-3, B-5, C-3	23.1	2.3203
AT1100C50D	400	27.30	1–2	A-3, B-5, C-3	26.1	2.4226
AT1100C50E	400	23.65	1–2	A-3, B-5, C-3	20.1	2.3031
AT1100C50F	400	25.21	1–2	A-3, B-5, C-3	30.8	2.3203

Since the density of steel remains the same after corrosion, volume loss is used to evaluate the corrosion rate in this study. The corrosion rates Ψ are calculated based on the weight of the steel tubes, seen in Equation (1), where A and A' denote the volume of the steel tube before and after corrosion, respectively. As shown in Table 4, the corrosion differs for specimens with the same ASTM evaluation results.

$$\psi = (A - A')/A\% \quad (1)$$

As can be obtained from the above equation, the ASTM method and weight evaluation method are unable to evaluate the corrosion sufficiently, thus fractal dimension was also used to evaluate the corrosion in this study. The differential box-counting approach proposed by Sarkar and Chaudhuri [20] was adopted based on 3D scanning profile results. Boxes of different sizes were used to overlap the volume of steel tubes that remained after corrosion, while the fractal dimension was calculated using Equation (2), where D is the fractal dimension, r is the edge length of box, and N is the number of boxes. It has been shown that there is linear relationship between $\log N(r)$ and $\log(1/r)$, such as specimen AT1100C50A in Figure 6, which illustrates that the corrosion has the fractal feature. The fractal dimensions of the corrosion of test specimens were calculated and presented in Table 4. It is shown that the fractal dimensions of corrosion were different for the specimens. It shows that the fractal dimension value generally increases with increasing corrosion

time for the CT series specimens, while the fractal dimension value exhibits a 5% variation though the specimens that have identical corrosion times. Meanwhile, the average value of a fractal dimension for the AT series specimens is 2.3487, which is close to that of the CT120 specimens, conveying that the fractal dimension of the atmospheric corrosion over three years is approximately equal to that of the chloride corrosion over about 120 days in this study.

$$D = \frac{\log N(r)}{\log(1/r)} \quad (2)$$

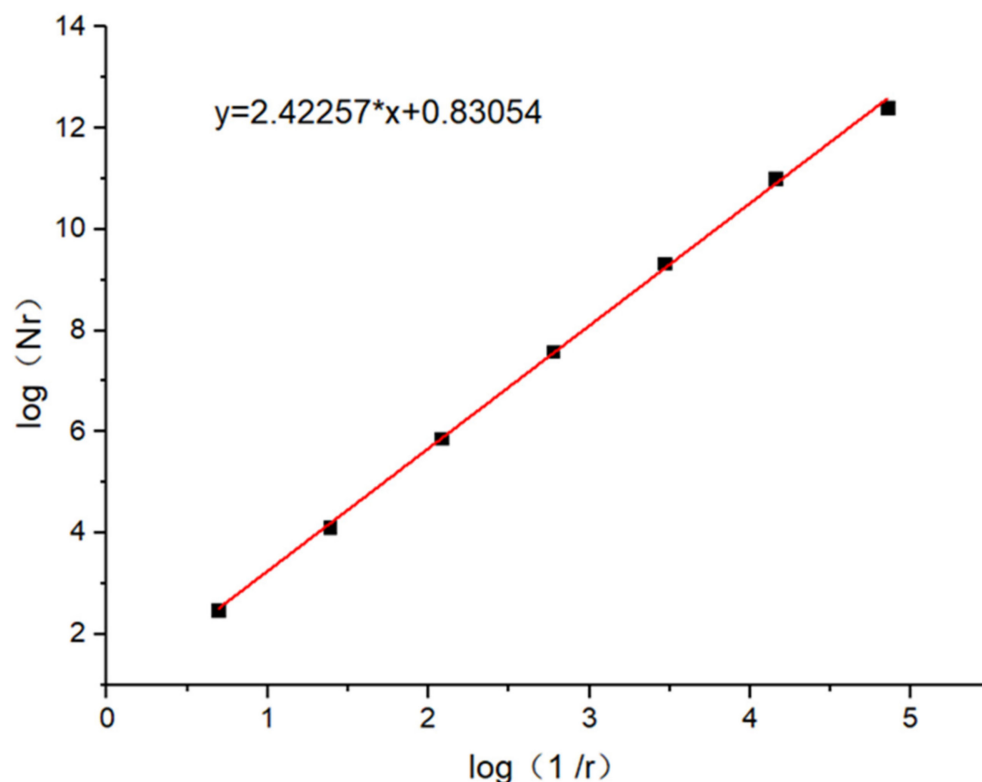
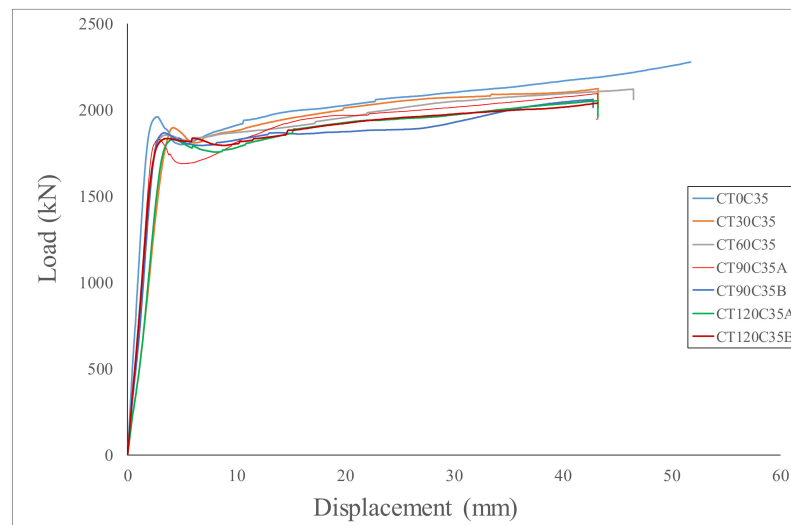


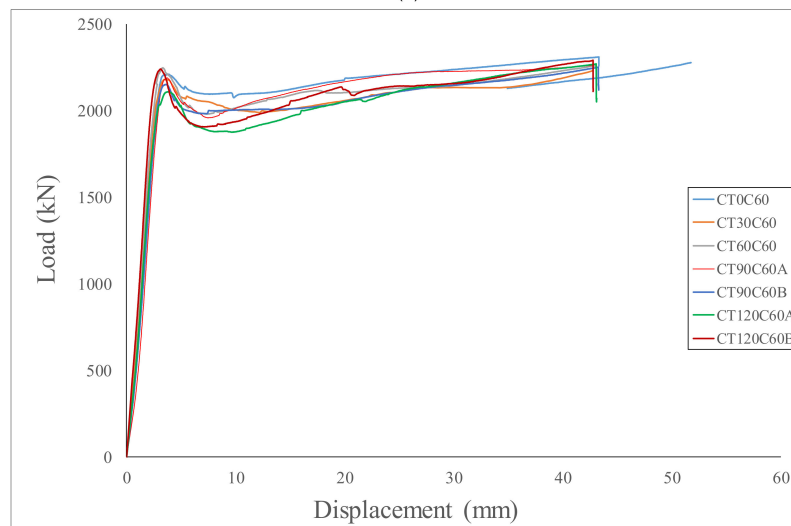
Figure 6. Fractal dimension of specimen AT1100C50A.

3.2. Loading Test Results

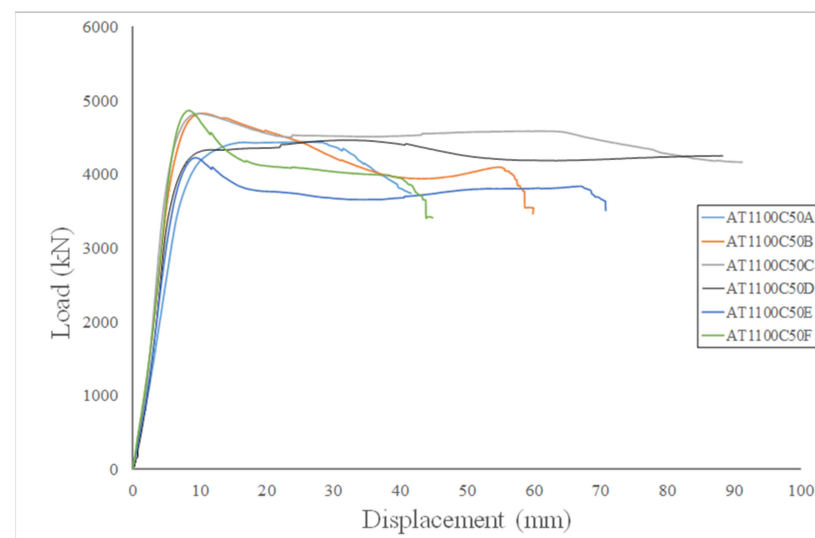
The load-displacement curves of the test specimens are plotted in Figures 7 and 8. Based on observation during the test process and the analysis of test data, the specimens are thought to experience two stages under loading. In the initial stage, the concrete and steel tube work together before reaching the first peak load. During the second stage, the load generally continues to increase after undergoing a short decrease. In the latter phase, large deformation of the steel tubes could be clearly observed as shown in Figure 9. It is worth mentioning that since the load increase in the second stage may lead to a cross-section increase for stub columns, the peak load in the first stage was considered the ultimate load in this study. If no peak load was found at the first test stage, the maximum load would be considered the ultimate load, as in AT1100C50C and AT1100C50D. Both of the small value differences between the repeated tests and the first value of each test set demonstrated the reliability of the test results, which has been presented in Table 5. It is shown that the corroded CFST specimens have a relatively lower ultimate load compared with the non-corroded counters, with up to a 10% reduction at most. A clear relationship between the ultimate load and corrosion rates has not been shown, which may relate to the variations in concrete strengths of specimens.



(a)



(b)

Figure 7. Load versus displacement curves of specimen CT series: (a) C35 Series; (b) C60 series.**Figure 8.** Load versus displacement curves of specimen AT series.

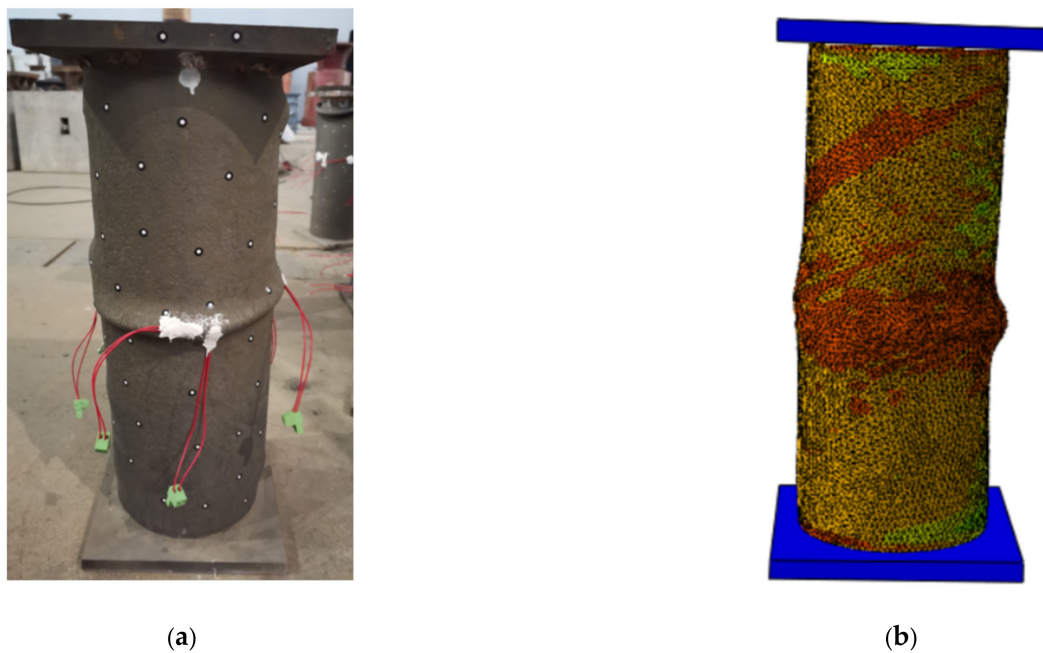


Figure 9. Comparison of failure mode of specimen CT90C35A: (a) test observed deformation; (b) FEA analysis deformation.

Table 5. Ultimate load comparison between test results and FEA results.

Specimens	P_{Test} (kN)	P_{FEA} (kN)	P_{Design} (kN)	P_{FEA}/P_{Test}	P_{Design}/P_{Test}
CT0C35	1960	1997	1237	1.02	0.63
CT0C60	2310	2250	1506	0.97	0.65
CT30C35	1897	1987	1237	1.05	0.65
CT30C60	2179	2390	1506	1.10	0.69
CT60C35	1829	1924	1237	1.05	0.68
CT60C60	2244	2109	1506	0.94	0.67
CT90C35A	1828	1898	1237	1.04	0.68
CT90C35B	1868	1892	1506	1.01	0.81
CT90C60A	2189	2292	1237	1.05	0.57
CT90C60B	2151	2274	1506	1.06	0.70
CT120C35A	1828	1898	1237	1.04	0.68
CT120C35B	1836	1845	1506	1.00	0.82
CT120C60A	2109	2244	1237	1.06	0.59
CT120C60B	2240	2272	1506	1.01	0.67
AT1100C50A	4438	4520	4170	1.02	0.94
AT1100C50B	4823	4722	4170	0.98	0.86
AT1100C50C	4781	4861	4170	1.02	0.87
AT1100C50D	4460	4500	4170	1.01	0.93
AT1100C50E	4222	4324	4170	1.02	0.99
AT1100C50F	4860	4785	4170	0.98	0.86
			Mean	1.02	0.75
			COV	0.035	0.169

The test observed that the steel tubes of columns, which experienced ultimate loading, eventually displayed final buckling failure. However, for test specimens AT1100C50A, AT1100C50B, AT1100C50E, and AT1100C50F, a fracture of the steel tube was observed at the second stage of the L-D curves, as seen in Figure 10. Displacements corresponding to their fracture point were 42 mm, 44 mm, 60 mm, and 70 mm for specimens AT1100C50A, AT1100C50B, AT1100C50E, and AT1100C50F, respectively. Generally, the fracture occurred at the welding, which suffers the most severe corrosion, as shown in Figure 10. As shown,

the welded steel tube is fractured due to the tensile stress caused by hoop expansion. Load versus average hoop strain curves of specimens from the AT series were plotted in Figure 11. Average hoop strains corresponding to their fracture points were 2912, 2584, 2232, and 3303 $\mu\epsilon$, respectively. The results demonstrate that corrosion has a significant effect on the ductility of the CFST column specimens with welded steel tubes. It should be noted that the effect of corrosion on the fracture of a steel tube due to horizontal tensile force has not been reported previously.



(a)



(b)



(c)



(d)

Figure 10. Cracks in corroded CFST specimens with welded steel tubes: (a) AT1100C50A; (b) AT1100C50B; (c) AT1100C50E; (d) AT1100C50F.

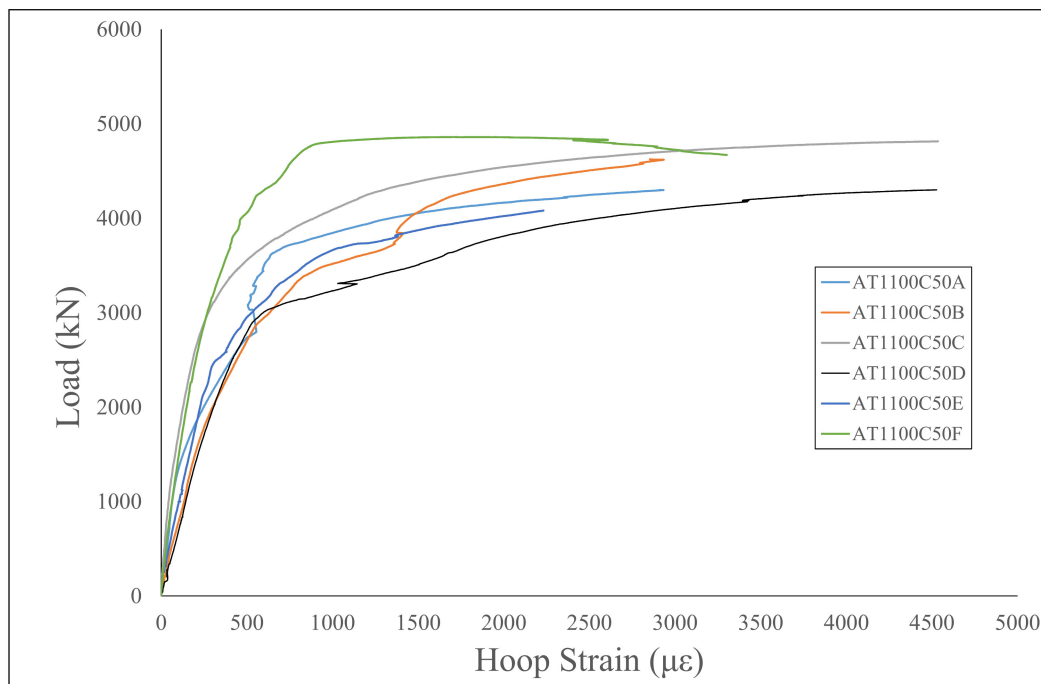


Figure 11. Load versus hoop strain curves of specimen AT series.

3.3. Comparison with Design Predictions

In order to investigate the suitability of the design equation for normal CFST columns for the corroded members, the design strengths of uncorroded specimens were predicted. Current AISC standards [21] and the design method proposed by Xu et al. [2] were used for the predictions. Table 5 has shown the compared results. It is found that the design predictions are conservative, especially for 480-mm CFST columns, which may be due to the end constraint effect [2], as shown in Table 5. The mean value and corresponding COV of $P_{\text{Design}}/P_{\text{Test}}$ are 0.75 and 0.169, respectively. Comparison indicated that the design equations for normal CFST columns are able to predict the column strengths of the corroded members in this study. Since the stub CFST columns are able to resist the compression load after yielding of steel tubes, the design predictions are conservative compared with the ultimate strengths obtained from the test results.

4. Finite Element Simulation

4.1. Finite Element Model

The finite element (FE) models were developed using ABAQUS/Standard [22]. Coordinate data obtained from the 3D scanning process were used to establish a model of the corroded steel tubes. The solid elements C3D8R were adopted for the steel end plate parts and the filled concrete, while the solid elements C3D10 were adopted for the steel tubes. The element size for the steel tube was approximately 1.0 mm, while the coarse mesh with an element size of 20 mm was used for concrete part. All degrees of freedom at both ends of the column specimens were fixed, except for the loading direction, as the boundary conditions in the test. Displacement was applied to the top end of the specimens to simulate the axial compression.

The true stress–strain curves obtained from the tensile coupon tests were used for the steel tubes. The constitutive model of steel was defined as von Mises yield criterion, associated with a flow rule with isotropic strain hardening [23,24]. The weld was assumed to have the same material properties as those of the steel. The concrete damaged plasticity model [22] was adopted for the concrete part. The equations suggested by Han et al. [25] were used to obtain the uniaxial compressive stress–strain relationship of the confined concrete. The Poisson’s ratio was taken as 0.2 for the infill concrete. A linear stress–strain

relationship was used for the concrete tensile behavior before reaching the tensile strength. For the concrete-to-steel surface-to-surface contact model, the hard contact behavior was set in the normal direction. In the tangential direction, the isotropic Coulomb frictions with a frictional factor of 0.6 [3] were adopted.

4.2. Verification

The deformations under the ultimate loads in the simulation were compared with the test results, as shown in Figure 9. Typical load versus displacement curves are compared in Figure 12. It is shown that the developed FE models were capable of predicting the initial stiffness and peak loads, while, for the plastic stage, a moderate discrepancy was observed, as shown in Figure 12. Ultimate strengths of the test and FE analysis are compared in Table 5. The average values of P_{FEA}/P_{Test} and the coefficient of variation (COV) were 1.02 and 0.035, respectively. In general, the established FE models incorporated with the steel fracture criterion can predict the mechanical behaviour of corroded CFST specimens with reasonable accuracy.

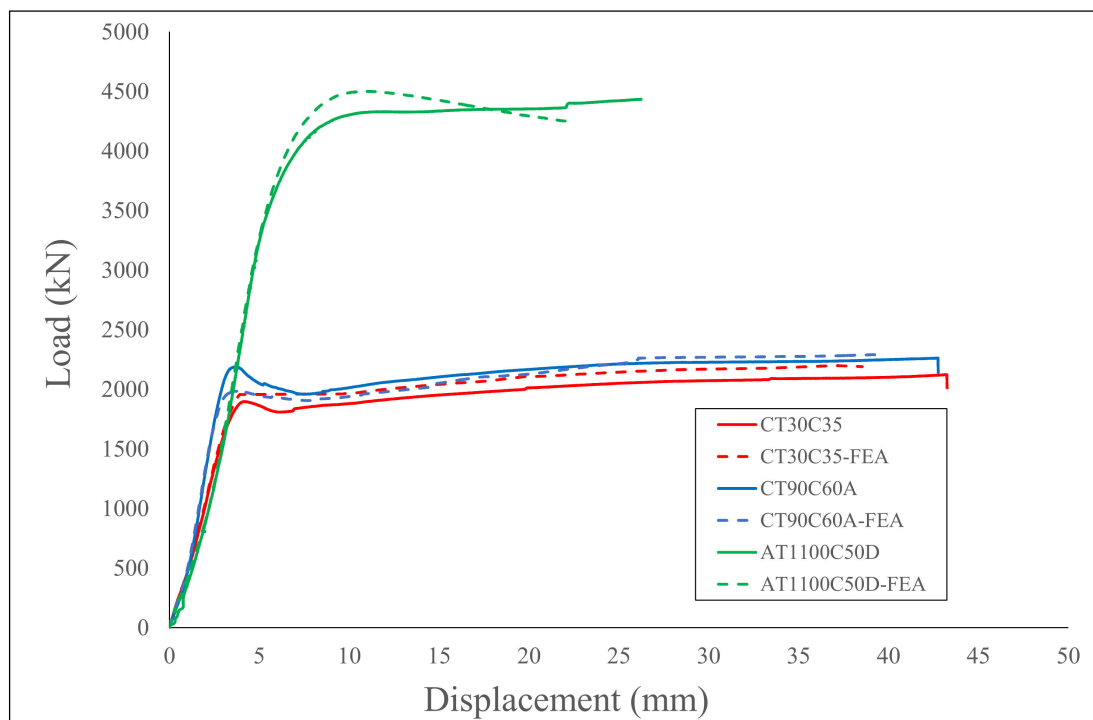


Figure 12. Comparison of typical load versus displacement curves.

4.3. Corrosion Pits Effect Analysis

For the uncorroded specimens, stress generally developed uniformly when the load increased, while those of the corroded ones were in non-uniform development, as shown in Figure 13. The stress states of test specimen AT1100C50A, corresponding to the 50% and 80% of ultimate load, are present in Figure 13a,b, respectively. The FEA simulation results in Figure 13a indicated that when the maximum stress reached a yield stress of 462 MPa, the minimum stress was only 330 MPa. The hoop strain states of specimen CT30C35 at points A, B, and C were obtained for illustration (shown in Figure 14). Point A is located in the center of the corrosion pit, and Point B is located inside the corrosion pit close to Point A. Point C is located in the uncorroded region. It is shown that stress distribution is obviously non-uniform. The hoop strain development at different points on specimens of CT30C35 can be seen in Figure 15. It is shown that the hoop strain develops rapidly when it reaches the yield load; then, the strain of Point A develops much faster than that of Point C.

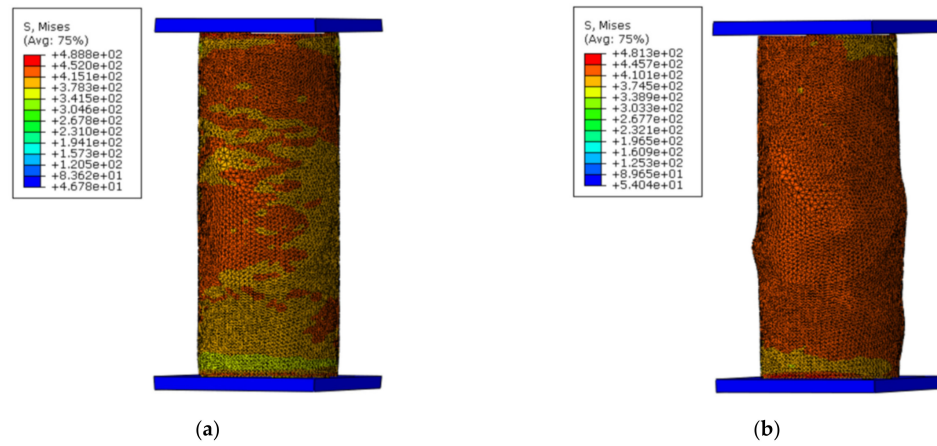
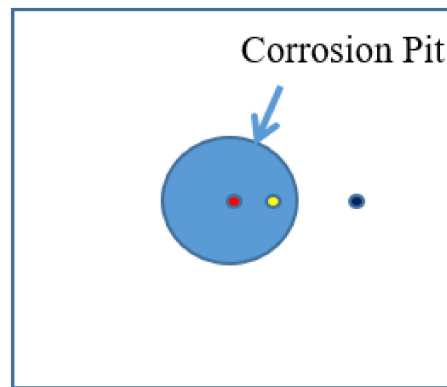


Figure 13. Stress development of specimen AT1100C50A: (a) 50% ultimate load; (b) 80% ultimate load.



● Point A ● Point B ● Point C

Figure 14. Illustration of Points A, B, and C.

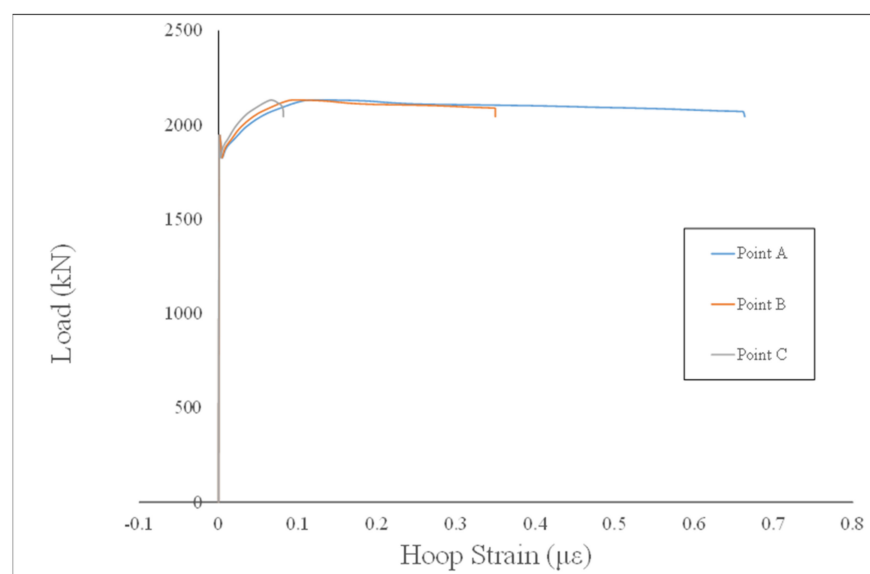


Figure 15. Hoop strain of different points on specimen CT30C35.

5. Conclusions

In this study, the compression behavior of the corroded CFST specimens was investigated by both a loading test and numerical method. Specimens that respectively suffered chloride ingress corrosion and atmosphere corrosion were examined, while a 3D scanning method was employed to obtain the profile of the steel tubes' surfaces. Corrosion evaluation was conducted based on the scanning results. It shows that the current ASTM method and the weight loss method are insufficient for estimation of the corrosion of test specimens. Therefore, a fractal method was developed for the corrosion evaluation in this study. Meanwhile, corrosion shows an effect on the ultimate strength of the CFST specimens in this study through exhibition of a reduction in the maximum strength of approximately 10%. However, corrosion may induce fracture of the welded steel tube under hoop expansion, which leads to a significant loss of ductility for these CFST pieces. Moreover, fracturing generally occurred at welding sites, which suffered the most severe corrosion. Furthermore, 3D scanning results to simulate the corrosion used in the finite element model show the developed method is available, and it presents a series of non-uniform stress versus strain curves of the steel tubes thanks to their corrosion condition. However, the high stress portion of the steel tube is able to resist the loading after its yielding until fracture. Therefore, design equation has access to predict the strengths of the generally corroded CFST stub columns in this study, and formulation for a safer operation of the analyzed structures should be developed in the future.

Author Contributions: Conceptualization, W.X., J.C. and F.X.; methodology, W.X. and F.X.; software, W.X.; validation, W.X., J.C. and F.X.; formal analysis, W.X.; investigation, W.X., C.Y. and C.L. resources, J.C. and F.X.; data curation, W.X. and F.X.; writing—original draft preparation, W.X.; writing—review and editing, F.X.; visualization, W.X.; supervision, J.C.; project administration, J.C.; funding acquisition, J.C. and F.X. All authors have read and agreed to the published version of the manuscript.

Funding: This research was funded by a grant of National Natural Science Foundation of China (grant number 52078249), the Key-Area Research and Development Program of Guangdong Province (grant number 2019B111107002), and International Science and Technology Program from Zhejiang Qinye Construction Industry Group Co., Ltd., 312000, China (grant number USX-UPC-2021330001000082).

Institutional Review Board Statement: Not applicable.

Informed Consent Statement: Not applicable.

Acknowledgments: The research work described in this paper was supported by a grant from the National Natural Science Foundation of China (52078249), the Key Area Research and Development Program of Guangdong Province (2019B111107002), and the International Science and Technology Program from Zhejiang Qinye Construction Industry Group Co., Ltd., Zhejiang 312000, China (USX-UPC-2021330001000082).

Conflicts of Interest: The authors declare no conflict of interest.

References

1. Young, B.; Ellobody, E. Experimental investigation of concrete-filled cold-formed high strength stainless steel tube columns. *J. Constr. Steel Res.* **2006**, *62*, 484–492. [[CrossRef](#)]
2. Xu, F.; Chen, J.; Jin, W.L. Experimental investigation of thin-walled concrete-filled steel tube columns with reinforced lattice angle. *Thin-Walled Struct.* **2014**, *84*, 59–67. [[CrossRef](#)]
3. Xu, F.; Chen, J.; Chan, T.M. Numerical investigation on compressive performance of CFST columns with encased built-up lattice-angles. *J. Constr. Steel Res.* **2017**, *137*, 242–253. [[CrossRef](#)]
4. Wang, Y.H.; Lu, G.B.; Zhou, X.H. Experimental study of the cyclic behavior of concrete-filled double skin steel tube columns subjected to pure torsion. *Thin-Walled Struct.* **2018**, *122*, 425–438. [[CrossRef](#)]
5. Xu, F.; Chen, J.; Guo, Y.; Ye, Y. Innovative design of the world's tallest electrical transmission towers. *Proc. Inst. Civ. Eng.* **2019**, *172*, 9–16. [[CrossRef](#)]
6. Xue, W.; Chen, J.; Xie, F.; Feng, B. Orientation of Steel Fibers in Magnetically Driven Concrete and Mortar. *Materials* **2018**, *11*, 170. [[CrossRef](#)]
7. Chen, J.; Wang, J.; Xie, F.; Duan, A. Behavior of thin-walled dodecagonal section double skin concrete-filled steel tubular beam-columns. *Thin-Walled Struct.* **2016**, *104*, 135–143. [[CrossRef](#)]

8. Chen, J.; Wang, J.; Xie, F.; Jina, W. Behavior of thin-walled dodecagonal section double skin concrete-filled steel tubes under bending. *Thin-Walled Struct.* **2016**, *98*, 293–300. [[CrossRef](#)]
9. Han, L.H.; Hou, C.; Wang, Q.L. Square concrete filled steel tubular (CFST) members under loading and chloride corrosion: Experiments. *J. Constr. Steel Res.* **2012**, *72*, 11–25. [[CrossRef](#)]
10. Han, L.H.; Hou, C.C.; Wang, Q.L. Behavior of circular CFST stub columns under sustained load and chloride corrosion. *J. Constr. Steel Res.* **2014**, *103*, 23–36. [[CrossRef](#)]
11. Han, L.H.; Hua, Y.X.; Hou, C.; Wang, Q.L. Circular Concrete-Filled Steel Tubes Subjected to Coupled Tension and Chloride Corrosion. *J. Struct. Eng.-ASCE* **2017**, *143*, 04017134. [[CrossRef](#)]
12. Hua, Y.X.; Han, L.H.; Wang, Q.L.; Hou, C. Behaviour of square CFST beam-columns under combined sustained load and corrosion: Experiments. *Thin-Walled Struct.* **2019**, *136*, 353–366. [[CrossRef](#)]
13. Hou, C.; Han, L.H.; Zhao, X.L. Full-range analysis on square CFST stub columns and beams under loading and chloride corrosion. *Thin-Walled Struct.* **2013**, *68*, 50–64. [[CrossRef](#)]
14. Xu, S.; Wang, Y.; Xue, Q. Evaluation indicators and extraction method for pitting corrosion of structural steel. *J. Harbin Inst. Technol. (NewSeries)* **2015**, *22*, 15–21.
15. Lv, S.; Mu, Q.; Gao, X. Influence of morphology of corrosion on fracture imitation in an aluminum alloy. *Mater. Des.* **2013**, *45*, 96–102. [[CrossRef](#)]
16. Li, S.L.; Xu, Y.; Li, H.; Guan, X. Uniform and Pitting Corrosion Modeling for High-Strength Bridge Wires. *J. Bridge Eng.* **2014**, *19*, 04014025. [[CrossRef](#)]
17. Xu, S.H.; Wang, H.; Li, A.B.; Wang, Y.; Su, L. Effects of corrosion on surface characterization and mechanical properties of butt-welded joints. *J. Constr. Steel Res.* **2016**, *126*, 50–62. [[CrossRef](#)]
18. AS 1391; Australian Standard. Methods for Tensile Testing of Metals. Standards Association of Australia: Sydney, Australia, 1991.
19. ASTM G46-94; Standard Guide for Examination and Evaluation of Pitting Corrosion. ASTM International: West Conshohocken, PA, USA, 2008.
20. Sarkar, N.; Chaudhuri, B.B. An efficient differential box-counting approach to compute fractal dimension of image. *IEEE Trans. Syst. Man. Cybern.* **1994**, *24*, 115–120. [[CrossRef](#)]
21. AISC 360; Specification for Structural Steel Buildings. AISC Committee on Specifications: Chicago, IL, USA, 2016.
22. Hibbitt, H.D.; Karlsson, B.I.; Sorensen, E.P. ABAQUS Documentation Collection, USA. 2010. Available online: <https://www.osti.gov/biblio/6459203-abaqus-epgen-general-purpose-finite-element-code-volume-example-problems-manual> (accessed on 18 March 2022).
23. Xu, L.Y.; Fan, J.S.; Yang, Y.; Tao, M.X.; Tang, Z.Y. An improved elasto-plastic constitutive model for the exquisite description of stress-strain hysteresis loops with cyclic hardening and softening effects. *Mech. Mater.* **2020**, *150*, 103590. [[CrossRef](#)]
24. Wang, C.; Fan, J.S.; Xu, L.Y.; Nie, X. Cyclic hardening and softening behavior of the low yield point steel: Implementation and validation. *Eng. Struct.* **2020**, *210*, 110220. [[CrossRef](#)]
25. Han, L.H. Flexural behavior of concrete-filled steel tubes. *J. Constr. Steel Res.* **2004**, *60*, 313–337. [[CrossRef](#)]